Supporting Information for

An observation of physisorption in high–performance FET–type oxygen gas sensor operating at room temperature

Seongbin Hong,[a] Jongmin Shin,[b] Yoonki Hong,[a] Meile Wu,[a] Dongkyu Jang,[a] Yujeong Jeong,[a] Gyuweon Jung,[a] Jong–Ho Bae,[a] Ho Won Jang[c] and Jong–Ho Lee*[a]

[a.] *Department of Electrical and Computer Engineering and Inter–University Semiconductor Research Center, Seoul National University, Seoul 08826, Republic of Korea.*

[b.] *Semiconductor R&D Center, Samsung Electronics Co., Ltd., Hwaseong, Gyeonggi 18448, Republic of Korea.*

[c.] *Department of Materials Science and Engineering and Research Institute of Advanced Materials, Seoul National University, Seoul 08826, Republic of Korea.*

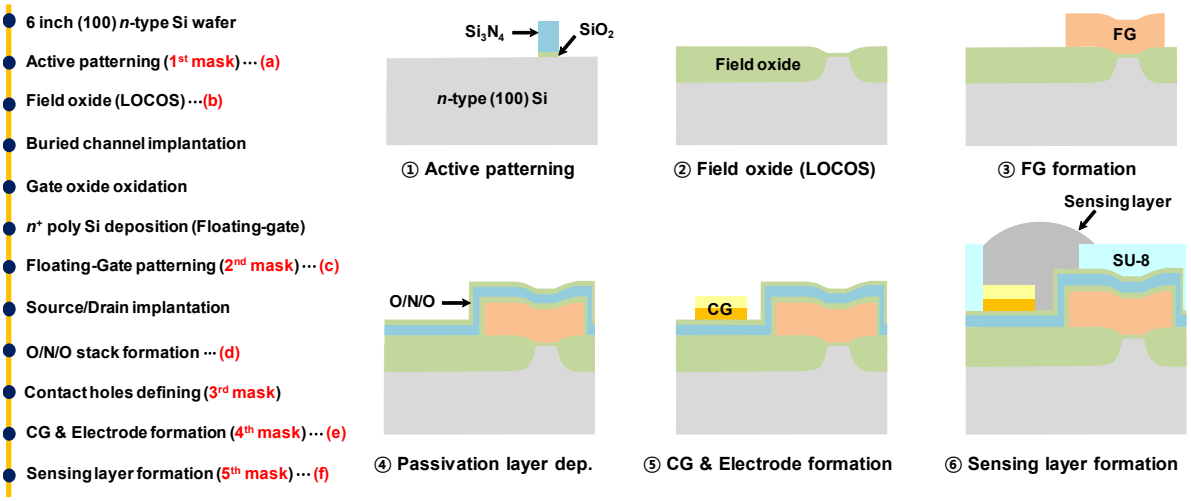

ESI Fig. S1. Key fabrication process steps of FET-type sensor.

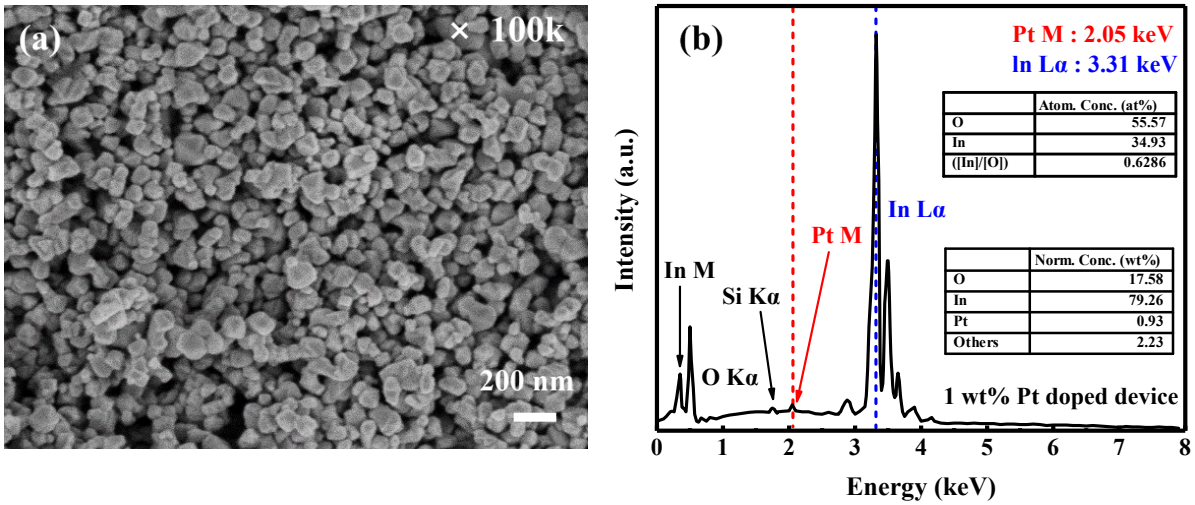

ESI Fig. S2. Characterization of the sensing material. (a) SEM micrograph (×100 k) and (b) EDS spectrum of the 1 wt% Pt–In_2O_3 nanoparticles.

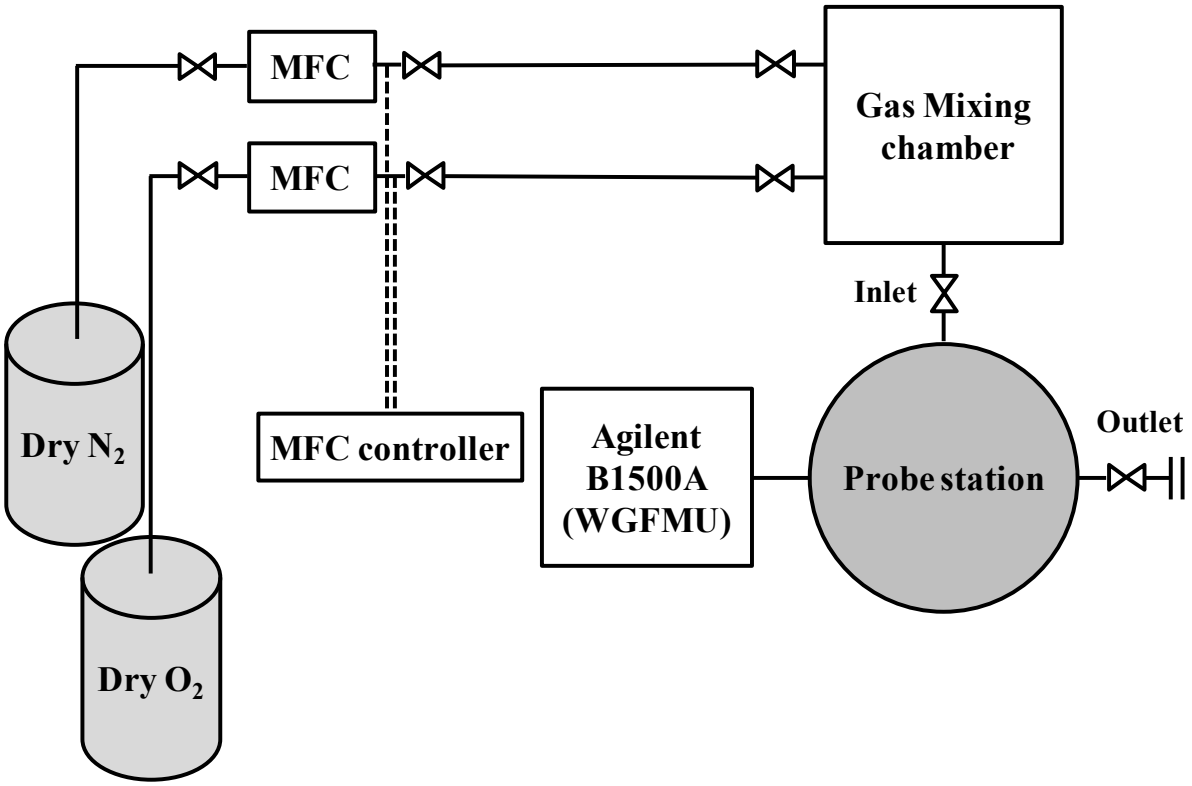

ESI Fig. S3. Schematic of the gas measurement system.

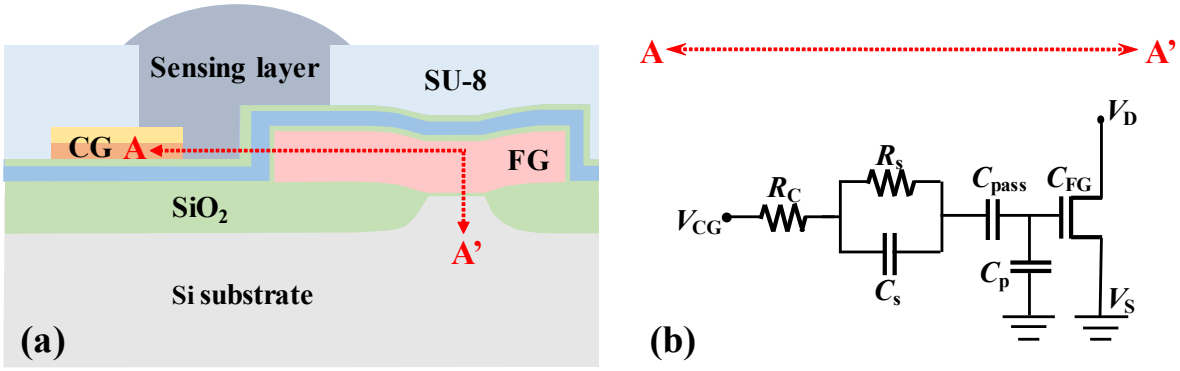

ESI Fig. S4. Equivalent circuit of FET-type sensor. (a) Cross-sectional schematic view cut along channel width direction. (b) Equivalent circuit of the device cut along A–A' in (a). R_C and R_s represent the resistances of the contact and sensing layer, respectively. C_s, C_{pass}, C_p, and C_{FG} denote the sensing layer capacitance, the capacitance between the sensing layer and the FG, the parasitic capacitance between the FG and the Si substrate, and the capacitance between the FG and the Si channel, respectively. Here, the overlap and fringing capacitances between the FG and the source/drain are ignored because they are too small.

Coupling ratio (γ)	$\dfrac{(\boldsymbol{C_s}//\boldsymbol{C_{pass}})}{(\boldsymbol{C_s}//\boldsymbol{C_{pass}}) + \boldsymbol{C_p} + \boldsymbol{C_{FG}}}$
Drain current (I_D)	$-\mu C_{FG}\dfrac{W}{L}\sqrt{\dfrac{\varepsilon_{si} q N_d}{4\varphi_B}}\left(\dfrac{kT}{q}\right)e^{-q\left(\lvert\gamma V_{CGS} - V_{th}\rvert\right)/mkT}$ **(subthreshold)**
	$\mu C_{FG}\dfrac{W}{L}\left(\lvert\gamma V_{CGS} - V_{th}\rvert + \dfrac{1}{2}V_{DS}\right)V_{DS}$ **(Linear)**

.

ESI Table S1. Formula of coupling ratio (γ) and drain current (I_D) in our FET-type sensor. Here, the effects of R_C ($\ll$1) and R_s ($\gg$1) in Supplementary Fig. 1(b) are ignored. In order to ensure high sensitivity, γ needs to be close to 1, which indicates that $C_s//C_{pass}$ should be much larger than C_p+C_{FG}. Because the CG and FG have an interdigitated pattern, the γ value of the platform sensor is generally higher than that of a conventional gas sensor having an air gap between the CG and the FG.

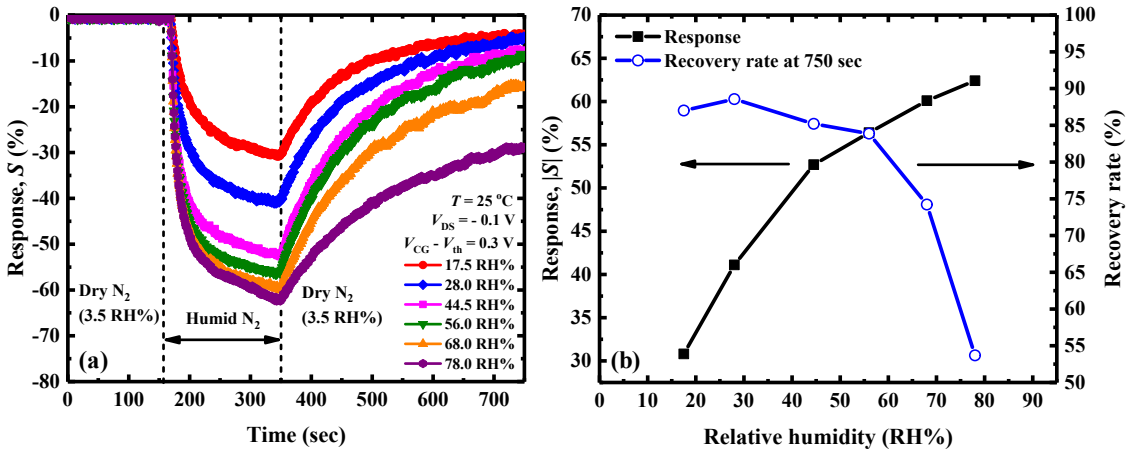

ESI Fig. S5. Humidity sensing characteristics in fabricated FET-type sensor. (a) Humidity responses of 1 wt% Pt-In_2O_3 FET-type sensor with relative humidity (RH) changed from 17.5 RH% to 78.0 RH% at room temperature (25 °C). V_{CG} - V_{th} is set to 0.3 V at V_{DS} = -0.1 V. (b) Humidity response versus RH%. As the RH% increases to 78.0 RH%, H_2O molecules act as an electron donor, and then work-function of the In_2O_3 layer decreases. As a result, $|I_D|$ decreases, resulting in decreasing response.

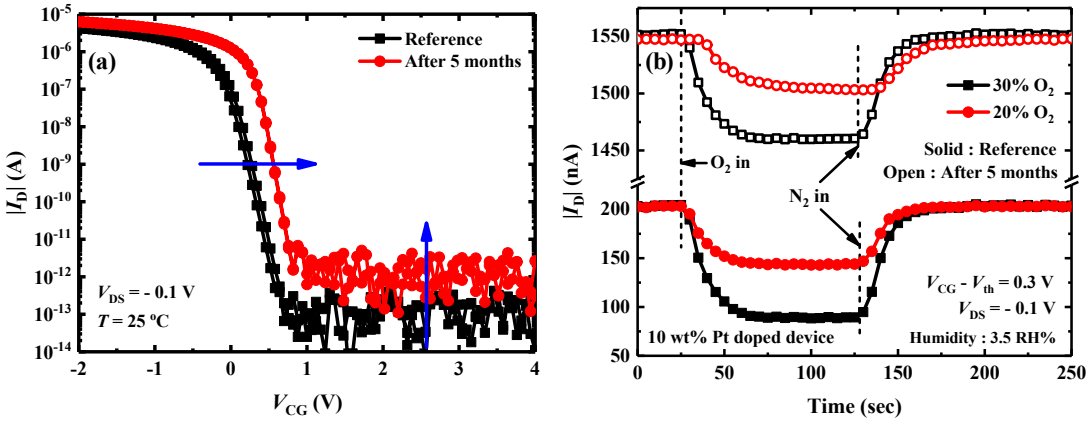

ESI Fig. S6. Stability of the fabricated FET-type sensor. (a) Transfer (I_D–V_{CG}) curves and (b) Transient responses to 20% and 30% O_2 gas measured after 5 months (red line) at 25 °C, compared to the reference (black line). After 5 months, the transfer curve in (a) shifts to the right and the off-current in (a) is increased by about 1 order. As a result, the reference I_D level is changed (~ 1.55 μA), but there is not meaningful difference in the O_2 sensing characteristics.

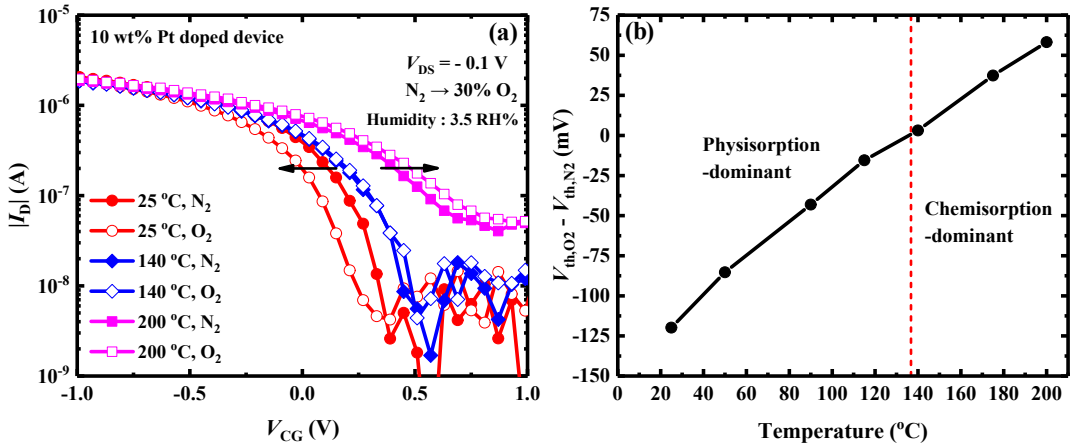

ESI Fig. S7. V_{th} change of FET-type sensor with temperature (T) change in O_2 ambience. (a) Transfer (I_D–V_{CG}) curves measured by applying V_{CG} pulses and (b) V_{th} changes for fabricated FET-type sensor in pure N_2 and 30% O_2 ambience as a parameter of T. At 25 °C, the transfer curve is shifted to the left when the chamber environment is changed from pure N_2 to 30% O_2. At 200 °C, on the other hand, the transfer curve is shifted to the right. These results demonstrate that T determines the dominance between the two sensing mechanisms, i.e., physisorption and chemisorption.

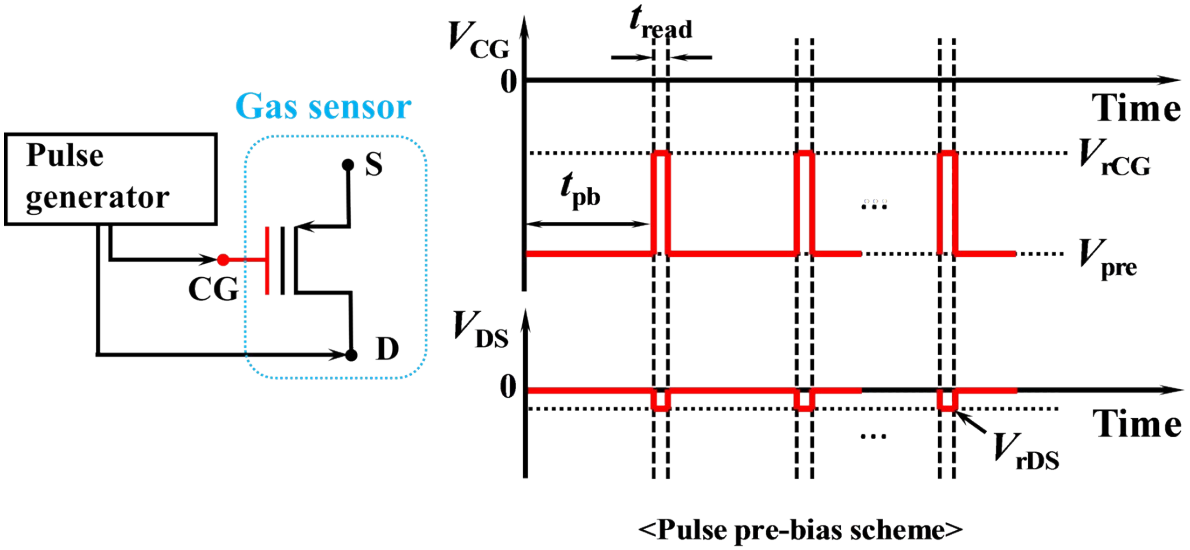

ESI Fig. S8. Pulse scheme to apply pre-bias to FET-type sensor. Control-gate and drain are biased by pulse generator, and source is grounded. Red line represents a series of pulses applied to the CG and drain. The pre-bias time (t_{pb}) and read pulse width (t_{read}) are fixed to 5 s and 500 μs, respectively.

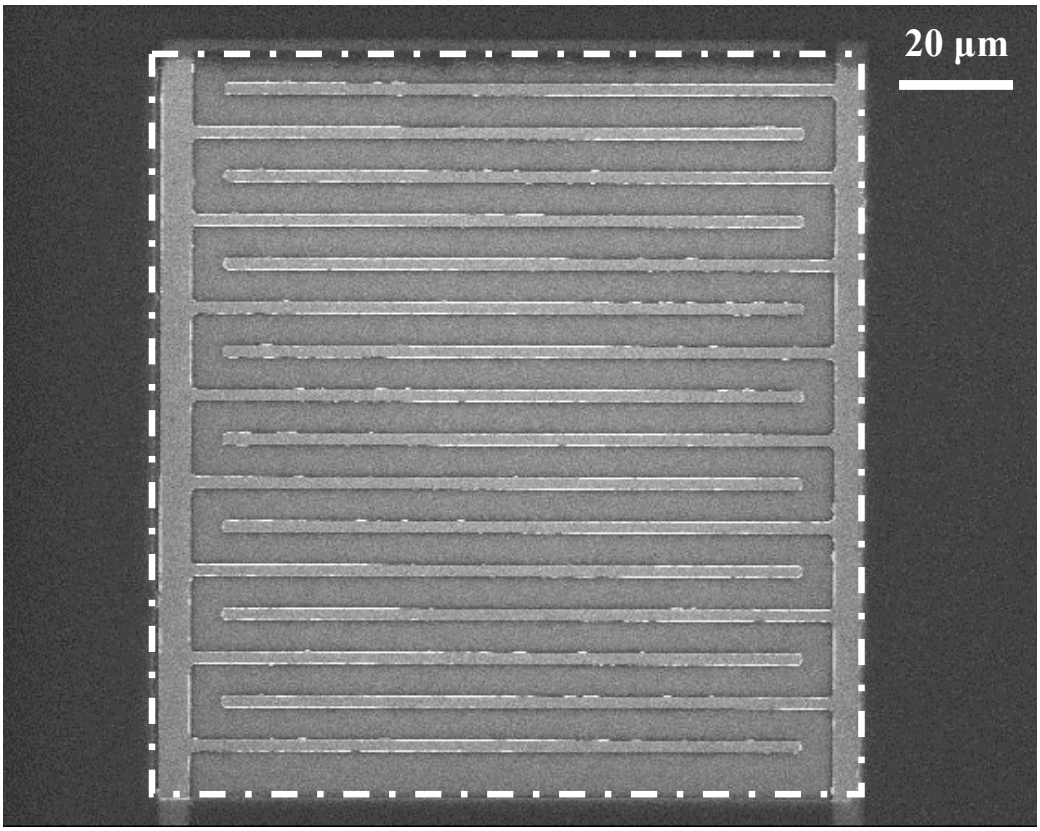

ESI Fig. S9. SEM image of the resistor-type sensor. The sensing layer prepared by inkjet-printing is indicated by a dash-dot line.

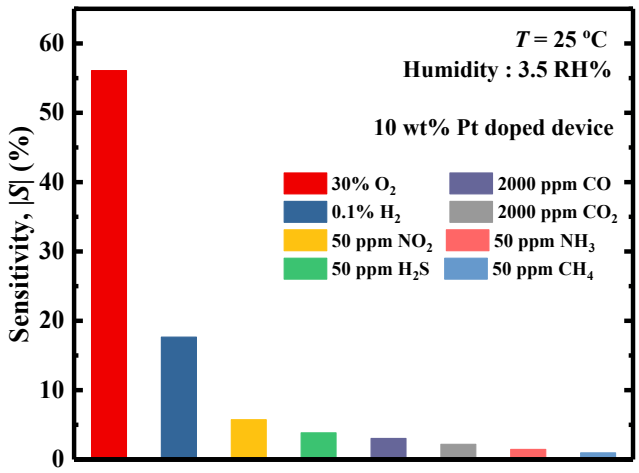

ESI Fig. S10. Responses of the fabricated sensor to the eight target gases (O_2, H_2, NO_2, H_2S, CO, CO_2, NH_3, and CH_4) at 25 °C in 10 wt% Pt–In_2O_3 sensor. The measurements are carried out in dry ambience.